Computers and Geotechnics 174 (2024) 106646

Contents lists available at ScienceDirect

Computers and Geotechnics

journal homepage: www.elsevier.com/locate/compgeo

Research Paper

An implicit material point-to-rigid body contact approach for large deformation soil–structure interaction

Robert E. Bird [a,*], Giuliano Pretti [a], William M. Coombs [a], Charles E. Augarde [a], Yaseen U. Sharif [b], Michael J. Brown [b], Gareth Carter [c], Catriona Macdonald [c], Kirstin Johnson [c]

[a] Department of Engineering, Durham University, South Road, Durham, DH1 3LE, UK
[b] School of Science and Engineering, University of Dundee, Fulton Building, Dundee, DD1 4HN, Scotland, UK
[c] British Geological Survey, Currie, Edinburgh, EH14 4BA, Scotland, UK

ARTICLE INFO

Dataset link: http://doi.org/10.15128/r1tt44pm87t

Keywords:
Material point method
Contact
Implicit
Soil–structure interaction
Large deformation mechanics

ABSTRACT

Modelling the interaction between rigid and deformable bodies holds significant relevance in geotechnical engineering, particularly in scenarios involving stiff engineering objects interacting with highly deformable material such as soil. These processes are challenging due to the combined nonlinear mechanisms including large deformation, elasto-plasticity, and contact with friction. For highly deformable material, the Material Point Method is a natural choice over the Finite Element Method due to its ability to handle large deformations without remeshing by carrying material information at points. This paper uses the Implicit General Interpolation Material Point Method (GIMPM) to demonstrate a new approach for modelling this type of interaction, and exploits the GIMPM's inherent definition of the boundary of a deformable domain to formulate a consistent contact formulation, negating the need for boundary reconstruction. The formulation is demonstrated through validations and comparisons to alternative methods for simulating contact. The combination of the contact formulation with an implicit framework is shown to be an efficient method for modelling geotechnical problems. The proposed method exhibits optimal convergence for contact problems, accurately captures stick–slip Coulomb friction, and ensures consistent stress fields at the contact surface of a rigid body.

1. Introduction

The ability to model the interaction between a rigid-body and deformable material is highly applicable to geotechnical engineering. In many processes there is a relatively very stiff engineering object interacting with a highly deformable material, such as a soil; for example Cone Penetration Tests (CPTs), pile and screw pile installation, seabed ploughing for cable installation and drag anchor trajectories in seabeds. However, modelling these engineering processes is challenging as there are multiple non-linearities: large deformation, elasto-plasticity and contact with friction. In terms of the numerical approach, the combination of these non-linearities makes these processes inherently difficult to model. A range of methods have been applied to these types of engineering problems, particularly to address the large deformation aspect. This includes, arbitrary Lagrangian Eulerian (ALE) finite element formulations, Tolooiyan and Gavin (2011) and Wang et al. (2015), particle finite element methods (Monforte et al., 2017; Hauser and Schweiger, 2021), discrete element methods (DEMs) (Ciantia et al., 2016; Khosravi et al., 2020), and the material point method (MPM) (Martinelli and Vahid, 2021). Here the MPM is used.

The MPM is a natural alternative to the finite element method, sharing many of the same numerical ingredients, but with the key advantages that no remeshing is required and the data for the problem are stored at locations in the domain (the material points, MPs) so it is not necessary to perform projections of historic material data, Coombs and Augarde (2020). Moreover, the MPM combines the advantages of a continuum particle-based formulation with the presence of a computational grid, which allows a Lagrangian solution approach. The governing equations are satisfied on an underlying background finite element mesh. The equilibrium equations governing continua modelled with the MPM and for a rigid body are well understood, the active area of research is how to couple the systems of equations through contact.

Before reviewing contact formulations in the MPM, it should be noted that contact in the MPM is closely aligned, but distinct to, the definition of boundaries and the imposition of homogeneous and inhomogeneous Neumann (traction) and Dirichlet (displacement) boundary

* Corresponding author.
E-mail address: robert.e.bird@durham.ac.uk (R.E. Bird).

https://doi.org/10.1016/j.compgeo.2024.106646

Available online 12 August 2024

conditions when the boundary is not aligned with the background grid. The representation of the external boundary of a MP-defined physical body has been achieved via B-Splines (Bing et al., 2019; Gavin, 2024), level sets (Liu and Sun, 2020) and proximity-based methods (Remmerswaal, 2017, 2023). However, for rigid body-MP interactions, a representation of the entire external boundary of the deformable MP body is not required; it is sufficient to have a representation of the contact surface between the two bodies, which can be provided by the discretisation of the rigid body. The imposition of inhomogeneous Neumann boundary conditions in the MPM has been explored by several authors. Most of these techniques require a discrete representation of the boundary of the body, for example (Bing et al., 2019; Gavin, 2024; Remmerswaal, 2023; Yamaguchi et al., 2021), with the notable exception of Liang et al. (2023) who used a virtual stress field to impose simple Neumann boundary conditions without explicit boundary representation. In many situations, Dirichlet boundary conditions can be imposed directly on the background grid via weak or strong enforcement methods and for some physical problems it is possible to define the background grid such that nodes of the background grid remain aligned with the boundary condition throughout the analysis, for example via the moving mesh concept (Phuong et al., 2016). However, there are many problems where it is not possible to align the boundary condition with the background mesh and this is a particular issue with the Generalised Interpolation Material Point Method (GIMPM), and B-Spline based MPMs that rely on a regular background grid. The imposition of non-grid-aligned Dirichlet boundary conditions in the MPM has been covered by Bing et al. (2019), Cortis et al. (2018) and Mast et al. (2011) and the reader is referred to Lu et al. (2019) for a review of these methods within different numerical schemes. However, the focus of this paper is the contact between a rigid body and a deformable body represented by MPs rather than imposing Neumann/Dirichlet conditions on the background grid.

Within the MPM community there are two active discussions regarding contact: how to represent the boundary of the domain and then how to enforce contact constraints on the boundary when the continuum data are stored at points. The nodal combined velocity-based method (NCVM) by Bardenhagen et al. (2000) is used by many authors (Gao et al., 2022; Ma et al., 2014; Bardenhagen et al., 2001; Chen et al., 2017; Gonzalez Acosta et al., 2021) because of its ease of implementation. This is because the interaction between bodies is imposed using the velocity fields at their interacting grid nodes. However, as discussed in Gonzalez Acosta et al. (2021) and Pretti (2024), the NCVM method has the potential for numerical dissipation because it does not satisfy the Karush–Kuhn–Tucker (KKT) conditions, which classically describe friction and contact (see, for instance, Simo and Laursen (1992)). Therefore, methods which do satisfy the KKT conditions are desirable since they are free from numerical dissipation, such as penalty (in the limit), augmented Lagrangian and Lagrange multiplier methods (Wriggers, 2006). The complexity of these methods is mainly due to the need for discretised surfaces, which is not a trivial task for the MPM (see Bing et al. (2019), Liu and Sun (2020) and Remmerswaal (2017)). A part of this intricacy can be avoided if the interaction takes place between a deformable MPM-discretised body and a rigid one, since the latter presents a geometrical description of the surface. In this regard, Ref. Nakamura et al. (2021) exploits the surface discretisation of an infinitely rigid body, while Lei et al. (2022) employs a finite element discretisation. As for the deformable body, a MP is either represented as a point (Lei et al., 2022), or a domain with a radius associated to its associated volume (Nakamura et al., 2021), which interacts with the body like a general point-to-surface method. When contact occurs, the normal and tangential contact forces are calculated at the point of contact and mapped to the background mesh nodes. An alternative method is to represent the rigid body as part of the grid boundary (Martinelli and Vahid, 2021). However, an unstructured mesh with remeshing is required as the shape moves and, like finite elements, it is distorted and hence inaccurate meshes are possible. Additionally, since this method requires irregular meshes, i.e. triangles in 2D, this is generally implemented using the MPM (Wang et al., 2021) rather than the GIMPM (Bardenhagen and Kober, 2004), the former exhibiting sub-optimal convergence properties for simple problems with regular background grids (Charlton et al., 2017) due to issues associated with "cell-crossing". There are other ways to mitigate the cell-crossing instability, such as using B-Spline based basis functions (Gan et al., 2018) and/or double mapping techniques (González Acosta et al., 2020), however GIMPM has other benefits linked to contact detection, which are outlined below.

The geotechnical application key in this paper is the modelling of cone penetration tests (CPTs) using the MPM, which has been achieved before by a number of authors using explicit-time integration schemes, for example (Martinelli and Vahid, 2021; Yost et al., 2023; Martinelli and Pisanò, 2022; Ghasemi et al., 2018; Bisht et al., 2021) amongst others. Generally explicit methods have been adopted over implicit methods due to ease of implementation and issues associated with poor integration of the background grid resulting in small contributions of material points to nodes of the background grid causing prohibitively poor conditioning numbers in the stiffness and mass matrices in implicit analysis. This issue is avoided by most explicit MPM implementations by the use of a lumped mass matrix and remapping/filtering of spurious nodal velocities via techniques such as Modified Update Stress Last (MUSL, Sulsky et al. (1995)), see Coombs (2023b) for a detailed discussion of this issue. However, the time period over which CPTs occur are generally long with small inertial effects (Robinson et al., 2021). When combined with the numerical aspect of requiring small elements around the cone tip, and the CFL (Courant–Friedrichs–Lewy) condition restricting the maximum time step, explicit analysis becomes less desirable due to the high number of time steps (requiring a high performance code for reasonable run times) and the adoption of artificial damping to approximate a quasi-static solution. Therefore an implicit, rather than explicit, pseudo-static analysis is the focus of this paper, with conditioning issues mitigated by the Ghost penalty method which will be explained below (Coombs, 2023b).

The main contribution of this article is a new implicit contact formulation for deformable/rigid interaction, based on some preliminary ideas outlined by Bird et al. (2023). GIMPM is used to model the deformable body which interacts with a discretised rigid body represented by a series of line segments. This is different to other material point contact approaches with rigid bodies. Hu et al. (2018) model the contact boundary condition at the material point position and therefore do not consider the volume associated with it. An improvement on this is provided by Nakamura et al. (2021), where the contact conditions are considered at a radius around a material point, where the radius approximates the material point's volume. There are also methods that use the boundary of the background mesh to represent the rigid body, see the works of Martinelli and Vahid (2021) and Martinelli and Galavi (2021), however this requires a triangular mesh that must be remeshed after a set number of load/time steps. The specific advantage of using the GIMPM over the MPM when modelling contact is that the shape of the deformable body is explicitly defined by the GIMPM domains associated with each MP and it is the boundary of this volume that governs the interaction with the rigid body. This choice has the added benefit that it avoids the reconstruction of a boundary representation of the deformable body. It also means that the contact constraints are consistent with the physical material, since the distance between the point of contact of the deformable body and that of the rigid body is based on the physical size of the GIMPM domain. An important added consequence of this approach is that accurate stress fields at the point of contact are obtained without additional processing/remapping. The final contribution of the paper is to demonstrate the benefits of using an implicit MPM to model large deformation soil–structure interaction, specifically applied to CPTs. Run times for an unoptimised serial MATLAB code, based on AMPLE (Coombs and Augarde, 2020), are used to demonstrate that accurate solutions for CPT analyses take

in the order of 10 min, whereas high fidelity models will take 30 min to an hour to obtain. The method is also validated against experimental data (Davidson et al., 2022) for homogeneous sands, and will be shown to reproduce features of CPTs in layered sands. Numerical examples demonstrate that the formulation is able obtain optimal convergence for contact problems, correctly capture stick–slip Coulomb friction, and for CPTs, to obtain consistent stress fields at the deformable body's contact surface.

2. Material point method

In this paper quasi-static large deformation mechanics is considered with isotropic elasto-plastic material behaviour. The material interacts with a rigid body with penalty normal contact and a regularised (penalty) slip–stick Coulomb friction law. The details of the implicit large deformation elasto-plastic MPM framework are presented in Coombs and Augarde (2020). The focus of this section is on the modification of the framework to allow rigid body interaction with the continuum material.

2.1. Equilibrium equations

Consistent with Coombs and Augarde (2020) and Charlton et al. (2017), and based on the observations of Coombs et al. (2020) regarding the compatibility of the MPM with different Lagrangian formulations, an updated Lagrangian framework is adopted in this paper. The weak statement for a material with domain, Ω, subject to body forces acting through the volume, V, and surface tractions acting over the boundary of the body, $\partial\Omega_N$, interacting with a rigid body via a contact surface $\partial\Omega_C$ is

$$\int_{\varphi_t(\Omega)} (\nabla_x \eta)_{ij}\sigma_{ij}dV - \int_{\varphi_t(\Omega)} \eta_i b_i dV - \int_{\varphi_t(\partial\Omega_N)} \eta_i t_i dS - \int_{\varphi_t^R(\partial\Omega_C)} \eta_i f_i dS = 0 \tag{1}$$

where φ_t is the motion of the deformable body, φ_t^R is the motion of the rigid body, η is the test function, σ_{ij} is Cauchy stress, ∇_x is the gradient operator in the updated coordinate system (denoted by the lower case x), b_i is the body force, t_i is the traction from Neumann boundary conditions and f_i is the normal and frictional forces imparted on the material from the interaction with the rigid body. The final term in (1) is the key difference in the equilibrium statement compared to that adopted in Coombs and Augarde (2020).

In order to discretise the problem a background mesh is introduced, which contains the continuous domain $\varphi_t(\Omega)$ at any point during an analysis. This background mesh, $\mathcal{T}$, is subdivided into a number of elements E. This allows the weak statement of equilibrium (1) to be expressed as

$$\sum_{E\in\mathcal{T}} \int_{\varphi_t(E)} (\nabla_x \eta)_{ij}\sigma_{ij}dV - \sum_{E\in\mathcal{T}} \int_{\varphi_t(E)} \eta_i b_i dV - \int_{\varphi_t(\partial\Omega_N)} \eta_i t_i dS - \int_{\varphi_t(\partial\Omega_C)} \eta_i f_i dS = 0. \tag{2}$$

Note that the surface traction and contact forces remain acting over the boundaries over which they act as they are not discretised by the background mesh. The next step is to introduce the basis (or shape) functions that provide the link between the vertices, v, of the background mesh and the material points, p, that discretise the physical domain. Several options are available in the MPM literature, including: conventional finite element shape functions used in the original MPM, generalised interpolation/CPDI basis functions that introduce a domain associated with each point, and B-spline basis functions (Sulsky et al., 1994; Bardenhagen and Kober, 2004; Sadeghirad et al., 2011). The research presented in this paper adopts generalised interpolation basis functions in order to mitigate the well known cell-crossing instability problem and adopts these functions for both the test and trial functions for the first term, and as the test function for the second term, in (2). The third and fourth terms in (2) adopt a test function based on the standard finite element shape functions of the background mesh, $[N]$, as these terms are not discretised by material points, instead they act as embedded boundary conditions within the mesh. The volume integrals in (2) are replaced by an assembly operator,[1] $\mathbf{A}$, over the material points representing the physical domain, each carrying an associated volume, V_p. This allows the weak statement of equilibrium to be expressed as a residual with the following form

$$\begin{aligned}\{R\} &= \mathop{\mathbf{A}}_{\forall p}\left([\nabla_x S_{vp}]^T\{\sigma_p\}V_p - [S_{vp}]^T\{b\}V_p\right) - \int_{\varphi_t(\partial\Omega_N)}[N]^T\{t\}dS \\ &\quad - \int_{\varphi_t(\partial\Omega_C)}[N]^T\{f\}dS \\ \{R\} &= \{f_{\text{int}}\} - \{f_{\text{b}}\} - \{f_{\text{t}}\} - \{f_{\text{c}}\}\end{aligned} \tag{3}$$

where $[\cdot]$ and $\{\cdot\}$ are a matrix and vector respectively, $[S_{vp}]$ is a matrix of basis functions for the element vertices, v, at each material point, p, and $\{\sigma_p\}$ is the Cauchy stress at a material point. The residual is a balance of the internal force associated with the material points' stress state, $\{f_{\text{int}}\}$, and the external actions acting on the body via: body forces, $\{f_{\text{b}}\}$, surface tractions, $\{f_{\text{t}}\}$, and contact forces, $\{f_{\text{c}}\}$.

In order to find the solution to Eq. (3) a Newton–Raphson (NR) scheme is used. The scheme requires the linearisation of (3) with respect to the primary unknown — the displacement of the background grid, $\{d\}$. The linearisation of the residual equation and applying the NR scheme gives

$$\{d\}_{i+1} = \{d\}_i - [K]_i^{-1}\{R\}_i \tag{4}$$

where i is the iteration number. The matrix $[K]$ is the linearised form of $\{R\}$, where only $\{f_{\text{int}}\}$ and $\{f_{\text{c}}\}$ are a function of the displacements of the background grid. The linearisation of $\{f_{\text{int}}\}$ for a single material point is

$$[k_p] = [\nabla_x S_{vp}]^T[A][\nabla_x S_{vp}]V_p \tag{5}$$

where $[A]$ is the algorithmic consistent material stiffness matrix. The global tangent stiffness matrix has the form

$$[K] = \mathop{\mathbf{A}}_{\forall p}\left([k_p] + [k_{\text{c}}]\right), \tag{6}$$

where $[k_{\text{c}}]$ is the tangent matrix for the contact force (normal and tangential), which is defined in the next section.

It should be highlighted that MPMs can suffer from the small cut problem due to the arbitrary nature of the interaction between the physical body (represented by material points) and the computational mesh used to solve the equilibrium equations, resulting in loss of coercivity of the linear system of equations (Sticko et al., 2020). In this work this issue is mitigated using Ghost stabilisation (Burman, 2010), first implemented in the MPM by Coombs (2023b). The key idea of Ghost stabilisation is to constrain the gradient of the solution within poorly populated elements of the background grid (i.e. those with small cuts) by introducing an additional coupling term integrated over the interface between these poorly conditioned elements and elements that are reasonably populated with material points. This introduces an additional term in the global tangent stiffness matrix with the form

$$[K_G] = \frac{\gamma_k h^3}{3}\int_\Gamma \left([G]^T[m][G]\right)d\Gamma, \tag{7}$$

where Γ denotes the collection of stabilised background element edges, h is the length of the stabilised edge, $[G]$ contains derivatives of the basis functions with respect to the global coordinates (but in a different format to $[\nabla_x S_{vp}]$), $[m]$ contains information about the normal

[1] Here the assembly operator, $\mathbf{A}$, is stating to perform this calculation at each material point and assemble their contributions to the degrees of freedom of the background grid nodes/vertices, v.

direction of the stabilised edge and γ_k is the Ghost stabilisation penalty parameter, usually defined as some proportion of the elastic stiffness.[2] The additional stiffness introduced by (7) enforces a bound on the minimum eigenvalue of the global tangent stiffness matrix and has been shown to significantly increase the robustness of implicit quasi static and dynamic MPM implementations for the analysis of single and bi-phase (solid-water) materials (Coombs, 2023b,a; Pretti et al., 2024). The physical implication of this additional stiffness is that the method stabilises non-physical, and potentially very large, displacements/velocities at the boundary of the physical domain caused by the imbalance between non-small internal/external force contributions and infinitesimally small mass/stiffness contributions to nodes of the background mesh. The definition of Γ is a key point of departure between cut-FEM (Sticko et al., 2020) and MPM (Coombs, 2023b) implementations, with the former determining the intersections of the physical boundary with the regular mesh, but this is not appropriate in the MPM as an explicit representation of the boundary is usually not available. Instead Coombs (2023b) defined Γ by: (i) identifying *boundary elements*, which are the elements attached to (sharing a face with) any unpopulated elements, and (ii) defining the *boundary element edges*, Γ, as the boundaries of these elements with other boundary elements or elements that are populated by material points. As Ghost stabilisation is a fix to a numerical artefact, the penalty stiffness (7) can be determined at the start of a load/time step rather than being recalculated at each iteration. This means that the associated force-like term of the weak form equilibrium equation can be determined from the product of (7) with the incremental background grid displacements (see Coombs (2023b) for details).

3. Contact

In this section the description of the contact of a GIMP domain with the rigid body is described. This starts first with a description of the rigid body, see Fig. 1. The rigid body is defined by its boundary L which is divided into straight segments l, as shown in Fig. 1. Each l has its own local coordinate $\xi \in [0, 1]$ and linear finite element shape functions $\hat{N}_1$ and $\hat{N}_2$. When a GIMP corner is in contact with the rigid body, highlighted in red, its position is defined $\boldsymbol{x}$ and is projected onto a line segment of the rigid body defined $\boldsymbol{x}'$ using the normal to l defined as n; details of the projection are defined in the next section.

The contact force residual $\{f_c\}$, (3), and its corresponding tangent $\{k_c\}$, (6), are formed from a normal, N, and tangential, T, contribution

$$\begin{aligned} \{f_c\} &= \{r_N^h\} + \{r_T^h\} \\ [k_c] &= [K_N^h] + [K_T^h]. \end{aligned} \tag{8}$$

The descriptions of the normal and tangential terms are respectively provided at the end of Sections 3.2 and 3.3.

3.1. Description of contact

The contact formulation presented here is inspired by the node-to-surface type contact formulations (Wriggers, 2006). Specifically we follow the work of Pietrzak and Curnier (1999) and modify their large deformation finite element-based framework the so that it can be applied to the MPM. The framework detailed in this paper is focused on a rigid body, represented by a mesh and termed the *main* body, interacting with a deformable continuum body represented by material points and termed the *secondary* body. The contact approach in this paper is therefore expressed as a (material) *point-to-surface* formulation to avoid any confusion with the nodes of the background mesh. Lastly, since the variables in this section are either scalars or vectors, a boldface notation is used from here on.

The numerical treatment of contact requires a number of ingredients to describe the normal and tangential nature of the contact interface, however the determination if contact is taking place is a critical first step. In this paper a closest point projection algorithm is used, this in turn enables the definition of the normal gap vector function $\boldsymbol{g}_n$ and gap function g_n

$$\begin{aligned} &\boldsymbol{g}_n(\xi(\tau), \tau) = g_n(\xi(\tau), \tau)\boldsymbol{n}(\xi(\tau), \tau) = \boldsymbol{x}(\tau) - \boldsymbol{x}'(\xi(\tau), \tau) \qquad \text{and} \\ &g_n = \boldsymbol{g}_n \cdot \boldsymbol{n}, \end{aligned} \tag{9}$$

which define the vector linking the interacting points on the main and secondary body and the length of this vector, respectively. In (9) $\boldsymbol{n}$ is the outward normal of the main body surface, $\boldsymbol{x}$ is the point in contact with the surface belonging to the secondary body, $\boldsymbol{x}'$ is the projection of $\boldsymbol{x}$ onto the main body surface, this being parameterised by a convective (local) coordinate, ξ. The scalar gap function, (9), allows three scenarios to be defined

$$g_n < 0, \quad \text{overlap}; \qquad g_n = 0, \quad \text{contact}; \qquad \text{and} \qquad g_n > 0, \quad \text{gap}. \tag{10}$$

The current form of the gap function in (9) provides only a normal description of the contact, a description of the tangential movement of a point over the surface that is consistent with (9) is also required. This description can be obtained by taking the time derivative of (9), which provides a description of the normal and tangential contact in rate form respectively denoted $\mathring{\boldsymbol{g}}_n$ and $\mathring{\boldsymbol{g}}_t$ (Curnier et al., 1995)

$$\begin{aligned} \dot{\boldsymbol{g}}_n(\xi(\tau), \tau) &= \dot{g}_n(\xi(\tau), \tau)\boldsymbol{n}(\xi(\tau), \tau) + g_n(\xi(\tau), \tau)\dot{\boldsymbol{n}}(\xi(\tau), \tau) \\ &:= \mathring{\boldsymbol{g}}_{\boldsymbol{n}}(\xi(\tau), \tau) + \mathring{\boldsymbol{g}}_{\boldsymbol{t}}(\xi(\tau), \tau) \\ &:= \mathring{\boldsymbol{g}}_{\boldsymbol{n}}(\xi(\tau), \tau) + \boldsymbol{t}(\xi(\tau), \tau)\dot{\xi}(\tau). \end{aligned} \tag{11}$$

In the Authors' opinion the component of $\mathring{\boldsymbol{g}}_{\boldsymbol{t}}$ has been written into a form that is simpler. It is composed of a tangent $\boldsymbol{t} = \partial \boldsymbol{x}/\partial \xi$, where ξ is the local coordinate of the element of that is contact with the point, and its rate $\dot{\xi}$.

Eq. (11) provides a description of the contact kinematics, next a definition of their variations is required as these will form the trial functions that compliment the normal and tangential forces on the MPs. Making use of the definitions in (11), these variations can be expressed as

$$\mathring{\boldsymbol{g}}_{\boldsymbol{n}}\delta t = \boldsymbol{n}\dot{g}_n\delta t = \boldsymbol{n}\delta g_n \qquad \text{and} \qquad \mathring{\boldsymbol{g}}_{\boldsymbol{t}}\delta t = \boldsymbol{t}\dot{\xi}\delta t = \boldsymbol{t}\delta\xi, \tag{12}$$

where the dependencies have been removed for readability. Unlike the previous section where the governing equations for the MPM were expressed directly via a weak form (see (1)), for the contact formulation it is instructive to start from a variational (or energy) form that distinguishes between the normal and tangential contact components. Within this context, and using the above definitions, the contact variational form of the contact energy for point-to-surface can be written as (Wriggers, 2006; Pietrzak and Curnier, 1999)

$$\delta U = \int_{\psi_t(\Omega)\cap\bar{\delta}(\boldsymbol{x}')} \left(\delta g_n \boldsymbol{n} \cdot \boldsymbol{p}_n + \delta\xi \boldsymbol{t} \cdot \boldsymbol{p}_t\right) \, \mathrm{d}x = 0 \tag{13}$$

where $\boldsymbol{p}_n$ and $\boldsymbol{p}_t$ are respectively the normal and tangential point forces. To define this as a point-to-surface contact the Dirac delta function is included in the integral, $\bar{\delta}(\boldsymbol{x}')$, at the projection point $\boldsymbol{x}'$. The normal and tangent contact components of (13) will be treated separately in the following sections. However, first a general description of the contact surface will be provided.

3.2. Normal contact

The approach detailed in this paper adopts a penalty method to approximately enforce the normal contact conditions. It is important

[2] Note that for dynamic analysis Ghost stabilisation can also be applied to the global mass matrix and in that case the penalty parameter is replaced by γ_M, which is usually defined as a proportion of the density of the material being analysed (Coombs, 2023b; Sticko et al., 2020).

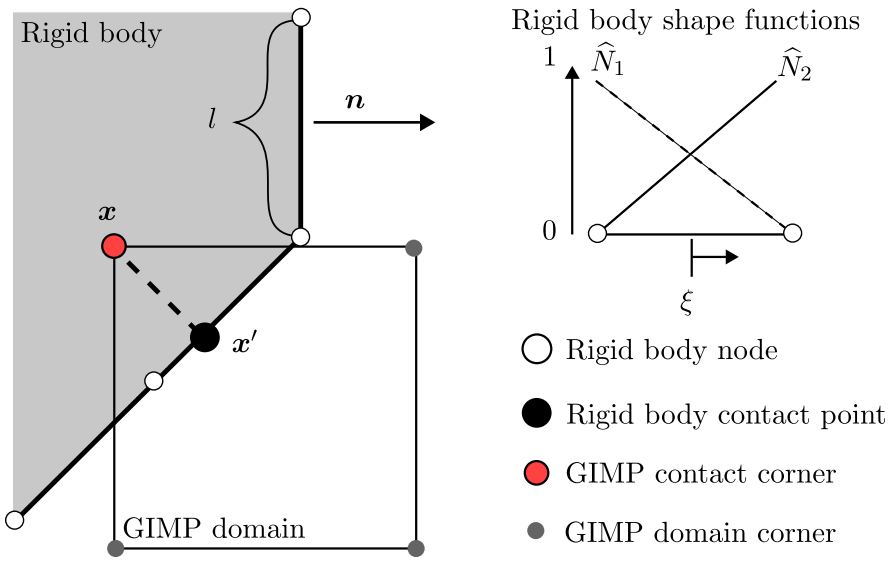

Fig. 1. A diagrammatic description of a GIMP in contact with the rigid body.

to note that penalty methods violate the Hertz-Signorini contact conditions (Pietrzak and Curnier, 1999)

$$g_n \geq 0, \qquad p_n \leq 0, \qquad \text{and} \qquad g_n p_n = 0 \tag{14}$$

and so, in general, some penetration will occur between the two bodies, with the magnitude of the penetration proportional to the penalty parameter.

To calculate the penalty force a normal penalty parameter is defined ϵ_n, which combined with the normal component of the gap function allows a normal penalty force to be defined as

$$\boldsymbol{p}_n = \boldsymbol{n} p_n \qquad \text{where} \qquad p_n = \epsilon_n g_n. \tag{15}$$

Substituting the penalty force from (15) into (13) and considering only the normal contact component, the variation for the normal residual can be determined. This variation is redefined as the residual that is solved to be zero in the Newton–Raphson loop,

$$r_N = \epsilon_n \int_{\psi_t(\Omega)\cap\bar{\delta}(\boldsymbol{x}')} \delta g_n \boldsymbol{n} \cdot \boldsymbol{n}\ g_n \ \mathrm{d}x = \epsilon_n \int_{\psi_t(\Omega)\cap\bar{\delta}(\boldsymbol{x}')} \delta g_n\ g_n \ \mathrm{d}x. \tag{16}$$

Linearisation of this residual in the direction $\Delta\boldsymbol{x}^h$ allows the stiffness associated with the normal contact component to be expressed as

$$K_N = \epsilon_n \int_{\psi_t(\Omega)\cap\bar{\delta}(\boldsymbol{x}')} \delta g_n\ \Delta g_n \ \mathrm{d}x. \tag{17}$$

Since the material is undergoing large deformation there is normally a second term in Eq. (17), corresponding to the degrees of freedom of the rigid body. However, in this paper it is assumed that the motion of the rigid body is defined and therefore this term is excluded from the linear system of equations, see Wriggers (2006) and Pietrzak and Curnier (1999) for details of this additional term.

In order to implement the contact approach, (16) and (17) need to be approximated with the MPM. This starts with the description of the variation of the test function, δg_n, and linearisation of the trial function, Δg_n, at the point $\boldsymbol{x}$,

$$\delta g_n = \{n\}[N(\boldsymbol{x})]^T\{\delta\boldsymbol{x}^h\} \qquad \text{and} \qquad \Delta g_n = \{n\}[N(\boldsymbol{x})]^T\{\Delta\boldsymbol{x}^h\} \tag{18}$$

where $[N(\boldsymbol{x})]$ is a matrix of shape functions corresponding the background grid at the position of the contact GIMP corner, $\boldsymbol{x}$. $\{\delta\boldsymbol{x}^h\}$ and $\{\Delta\boldsymbol{x}^h\}$ are the respectively the test and trial constants at the background grid nodes associated with the shape functions $[N(\boldsymbol{x})]$. $\{\boldsymbol{n}\}$ is the outward normal to the rigid body surface.[3] Substituting (18) into (16) and (17), integrating, and removing the test function coefficients, gives the discretised forms the residual,

$$\{r_N^h\} = \epsilon_n[N(\boldsymbol{x})]\{\boldsymbol{n}\}^T g_n, \tag{19}$$

and the tangent matrix,

$$[K_N^h]\{\Delta u^h\} = \epsilon_n[N(\boldsymbol{x})]\{\boldsymbol{x}\}^T\{\boldsymbol{x}\}[N(\boldsymbol{x})]^T\{\Delta u^h\}. \tag{20}$$

3.3. Tangential contact

The tangential component of the contact conditions follow a similar approach to that outlined for the normal contact conditions. The residual for the tangential contact component from (13) can be expressed as

$$r_T = \int_{\psi_t(\Omega)\cap\bar{\delta}(x_i')} \delta\xi \boldsymbol{t} \cdot \boldsymbol{p}_t \ \mathrm{d}x. \tag{21}$$

To simplify (21), it can be noted that $\boldsymbol{p}_t$ can be expressed as a function of the tangent $\boldsymbol{t}$ and a scalar component p_t,

$$\boldsymbol{p}_t = p_t \boldsymbol{t} \quad \text{and} \quad p_t = \boldsymbol{t} \cdot \boldsymbol{p}_t. \tag{22}$$

Subsisting the Equations in (22) into (21) gives the residual as

$$r_T = \int_{\psi_t(\Omega)\cap\bar{\delta}(x_i')} \delta\xi p_t \ \mathrm{d}x \tag{23}$$

and its linearisation in the direction $\Delta\boldsymbol{x}^h$ as

$$K_T = \int_{\psi_t(\Omega)\cap\bar{\delta}(x_i')} \delta\xi \Delta p \ \mathrm{d}x. \tag{24}$$

Similarly to (17) an additional term in (21) where the rigid body is free to move is neglected in this paper. The general derivation of the $\delta\xi$ term is omitted for the sake of brevity; see Pietrzak and Curnier (1999) for details. Since the motion of the rigid body is prescribed and the body is formed from straight edges, and locally the surface of the body is one-dimensional, $\delta\xi$ has the form

$$\delta\xi = A\delta\boldsymbol{x} \cdot \boldsymbol{t} \quad \text{where} \quad A^{-1} = (\boldsymbol{t} \cdot \boldsymbol{t}). \tag{25}$$

[3] Note that the notation has changed to matrix/vector form due to the change of focus from the definition of the contact equations to implementation of the approach in the material point method.

In order to discretise (28) and (29), the discrete form of $\boldsymbol{t}$ is necessary, which takes the form

$$\boldsymbol{t}_h = [B^{\xi}(\boldsymbol{x})]\{\boldsymbol{x}_h\}, \tag{26}$$

where $[\widehat{B}(\boldsymbol{x}')]$ is a matrix of shape function derivatives of the rigid body element on which $\boldsymbol{x}'$ resides, see Fig. 1. Explicitly $[\widehat{B}(\boldsymbol{x}')]$ has the form

$$[\widehat{B}(\boldsymbol{x}')] = \begin{bmatrix} \frac{\partial \widehat{N}_1(\boldsymbol{x}')}{\partial \xi} & 0 & \frac{\partial \widehat{N}_2(\boldsymbol{x}')}{\partial \xi} & 0 \\ 0 & \frac{\partial \widehat{N}_1(\boldsymbol{x}')}{\partial \xi} & 0 & \frac{\partial \widehat{N}_2(\boldsymbol{x}')}{\partial \xi} \end{bmatrix}, \tag{27}$$

where $\widehat{N}$ are the shape functions for the segment l and are not associated with the MP background grid. The discrete forms of (28) and (29) can now be expressed as

$$\{r_T\} = A[N(\boldsymbol{x})][\widehat{B}(\boldsymbol{x}')]\{\boldsymbol{x}_h\}p_t, \tag{28}$$

and

$$[K_T]\{\Delta \boldsymbol{x}_h\} = A[N(\boldsymbol{x})][\widehat{B}(\boldsymbol{x}')]\{\boldsymbol{x}_h\}\left[\partial p_t/\partial x\right]\{\Delta \boldsymbol{x}_h\}, \tag{29}$$

where $\left[\partial p/\partial x\right]$ is the derivative of the frictional force with respect to the position of the contact point, $\boldsymbol{x}_h$, and is discussed in the next section.

3.4. Friction

The vector of the total path of point over a surface is denoted by $\boldsymbol{g}_t$ and comprises two parts: (i) the tangential slip, $\boldsymbol{g}_{slip}$, which is purely dissipative and forms the plasticity component of the friction model, and (ii) the tangential stick, $\boldsymbol{g}_{stick}$. Here we use an elastic law, or penalty method, to describe the force corresponding to $\boldsymbol{g}_{stick}$, therefore $\boldsymbol{g}_{stick}$ can be described as the purely elastic, recoverable motion of the particle along the surface. If we were to remove the tangential force holding the particle in place by maintaining the normal force, the particle would move to set $\boldsymbol{g}_{stick} = \boldsymbol{0}$. These components can be described with the equation

$$\boldsymbol{g}_t = \int_T \mathring{\boldsymbol{g}}_t \, \mathrm{d}t = \int_T \mathring{\boldsymbol{g}}_{slip} \, \mathrm{d}t + \int_T \mathring{\boldsymbol{g}}_{stick} \, \mathrm{d}t = \boldsymbol{g}_{slip} + \boldsymbol{g}_{stick}, \tag{30}$$

where T is the total contact time. As a penalty method is used to describe the stick state, the relationship between the stick force acting on the main surface, $\boldsymbol{p}_{stick}$, and $\boldsymbol{g}_{stick}$ is

$$\boldsymbol{p}_{stick} = \epsilon_t \boldsymbol{g}_{stick}. \tag{31}$$

For the slip component the classical[4] Coulomb stick–slip friction law is used, the law takes the form,

$$\boldsymbol{p}_t = \mu|p_n| \frac{\mathring{\boldsymbol{g}}_{slip}}{\|\mathring{\boldsymbol{g}}_{slip}\|} \qquad \text{if} \qquad \|\boldsymbol{p}_{stick}\| > \mu|p_n|, \tag{32}$$

where $\mu|p_n|$ is the sticking force. The law is subject to the Karush–Kuhn–Tucker (KKT) conditions, applied in a similar way to plasticity

$$f = \|\boldsymbol{p}_{stick}\| - \mu p_n \leq 0, \qquad \lambda \geq 0 \qquad \text{and} \qquad f\lambda = 0, \tag{33}$$

where f is the frictional yield function, λ is the yielding rate, and the constitutive evolution of the plastic slip is

$$\mathring{\boldsymbol{g}}_{slip} = \frac{\partial f}{\partial \boldsymbol{p}_{stick}} = \lambda \frac{\boldsymbol{p}_{stick}}{\|\boldsymbol{p}_{stick}\|}. \tag{34}$$

In order to be implemented within the material point modelling framework the continuous form of these friction equations need to be reformulated into the pseudo-static problem with incremental sliding, and a method to determine the tangential forces and the sliding state (stick-or-slip) needs to be defined. The overall approach taken in this paper is:

1. Using a elastic trial state, determine if the point is in a stick or slip state.
2. Based on the contact state:
   (a) Stick: If the state is within the yield surface, calculate the stick force.
   (b) Slip: If the state is outside the yield surface, map the state back onto the yield surface and calculate the slip force;
3. Store all the history dependent components for load step of the global algorithm.

The elastic trial state requires a definition of the incremental slip, $\Delta \boldsymbol{g}_t$. This is calculated from the backward-Euler (pseudo) time discretisation of tangential velocity $\mathring{\boldsymbol{g}}_t$, giving

$$\begin{aligned} \mathring{\boldsymbol{g}}_t \Delta t &\approx \boldsymbol{g}_t^{m+1} - \boldsymbol{g}_t^m \\ &= \boldsymbol{t}^{m+1} \Delta \xi = \boldsymbol{t}^{m+1}(\xi^{m+1} - \xi^m) \\ &= \Delta \boldsymbol{g}_t \end{aligned} \tag{35}$$

where m is the load step. There are a couple algorithmic notes here, first it is important to note that the surface tangent $\boldsymbol{t}^{m+1}$ corresponds to the current tangent. Second, ξ^{m+1} and ξ^m both correspond to the coordinate system of the current rigid body element that the point projects onto. The point ξ^m is therefore determined using a CPP of the converged position of the point $\boldsymbol{x}'$ at step m, onto the current element's converge position also for step m. The calculation ξ^m is unaffected by whether in step m the point was in contact or not.

With the definition (35) it is now possible to defined the elastic trial state as

$$\boldsymbol{p}_{tr} = \epsilon_t(\boldsymbol{g}_t^{m+1} - \boldsymbol{g}_{slip}^m) \tag{36}$$

where $(\boldsymbol{g}_t^{m+1} - \boldsymbol{g}_{slip}^m)$ is the trial stick movement that has occurred. However, since the friction coefficient μ in Eq. (33) is constant, the elastic trial state can be expressed as

$$\boldsymbol{p}_{tr} = \boldsymbol{p}_t^m + \epsilon_t \Delta \boldsymbol{g}_t. \tag{37}$$

This is simpler from an algorithmic point of view because only the previously converged tangential sliding force, $\boldsymbol{p}_t^m$, needs to be stored as a historic variable. Additionally, since μ is constant $\boldsymbol{p}_{tr}$ the calculation of λ is direct and defined as,

$$\lambda = \frac{1}{\epsilon_t}\left(\|\boldsymbol{p}_{tr} - \mu p_n^{m+1}\|\right). \tag{38}$$

Finally, the updated tangential force can be calculate as

$$\boldsymbol{p}_t^m = \begin{cases} \boldsymbol{p}_{tr} & \text{if} \quad f \leq 0, \quad \text{stick} \\ \mu|p_n|\left(\boldsymbol{p}_{tr}/\|\boldsymbol{p}_{tr}\|\right) & \text{if} \quad f > 0, \quad \text{slip} \end{cases} \tag{39}$$

It is important to note that the trial state $\boldsymbol{p}_{tr}$ is used to compute the direction for the frictional for both the slip and stick states. This can be confirmed by the backward Euler integration of (34) and noting that the direction of the trial and elastic tangential forces are the same (Wriggers, 2006).

3.5. Determining the contact penalty parameters

The normal and tangential contact conditions require the penalty parameters, ϵ_n and ϵ_t, to be chosen such that interpenetration and movement during stick, are small. Additionally ϵ_n and ϵ_t need to have values that are consistent with the surface area of contact that is being represented by the point load. For the normal contact, this means that ϵ_n is calculate using the expression

$$\epsilon_n = \gamma A_p E_p, \tag{40}$$

where E_p is the Young's modulus of the material point, γ is a scaling parameter with units m^{-1}, and A_p is the area of contact associated with the material point p. This is defined in plane-strain problems as the diameter of the circle that encompasses the GIMP domain multiplied by a unit length for the out-of-plane dimension. For axisymmetric problems it is the same diameter multiplied by the original radial position of the GIMP. Through empirical observation it was found that setting $\epsilon_t = \epsilon_n/2$ produced a consistently stable Newton–Raphson algorithm.

[4] Classical since the friction coefficient μ is constant.

3.6. Single load step algorithm

An aspect of contact that makes it undesirable for implicit methods is the potential lack of convergence. Therefore in this section the algorithm use to solve the global system of equations with contact is presented, later in the numerical section typical convergence for solving real problems is demonstrated. The solution algorithm can be summarised as:

1. **Initialise**:
   (a) Increment the position of the rigid body for this new load step.
2. **Contact Detection and Point Listing**:
   (a) Identify points that can be in contact and create contact list.
3. **Newton–Raphson scheme**:
   (a) Use the Newton–Raphson scheme to solve the system of equations.
   (b) The contact list from 2(a) is unchanged.
4. **Contact Detection and Point Update**:
   (a) Perform a contact search, and determine if new points have come into contact.
   (b) If applicable, update the list of points that are in contact.
5. **Convergence Check**:
   (a) If the updated list of points contains no new contact points the algorithm terminates as convergence is achieved.
   (b) Otherwise, return to step 2 and repeat the process.

The main aspect that can causes convergences are points coming in and out of contact, this fundamentally changes the system of equations being solved. We therefore solve a load step in several steps. First, contact is detected and all the points that are in contact are listed. Second, the Newton–Raphson scheme is used to solve the system of equations with the list of points that are potentially in contact unchanged from the first step, this acts to reduce how much the system of equations can change. Once the system has been solved a post solve detection stage is performed 4(a)–(b), this is necessary since new points may be in contact and hence their contact also needs to be resolved for this load step. If the list does not contain new contact points the first stage of the algorithm finishes, otherwise the algorithm goes back to the Newton–Raphson scheme with this new list of contact points.

4. Numerical simulations

In this section the results of several numerical experiments are presented, they are ordered in complexity to demonstrate the efficacy of each component of the contact algorithm. The first two numerical experiments validate the methodology of the using the corners of the GIMP domain for the normal and tangential contact:

1. Validation of the normal contact to demonstrate that the point contact on the corners of the GIMP domains produces a consistent stress field.
2. A stick–slip friction experiment to confirm the efficacy of employing the GIMP domain corners and the stick–slip algorithm outlined in Section 3.4 for tangential contact.

The next two experiments are of real-world example use of the algorithm, with a comparison to experimental data. These experiments will show that the MPM-rigid body contact produce accurate results, but also that the implicit approach achieves good run-times in an unoptimised serial MATLAB implementation based on AMPLE (Coombs and Augarde, 2020) with Ghost stabilisation (Coombs, 2023b), but also the good performance of the non-linear solver presented in Section 3.6 for these real world examples:

3. CPT validation: comparison between the numerical results and those obtained experimentally in homogeneous dry sand for two relative densities with a range of mesh resolutions.
4. CPT algorithmic performance: an investigation of the impact of the material point density on the predicted CPT response and the stability of the contact algorithm.
5. CPT in layered soils: demonstrate that the method is able to model the more realistic case of layered soil profiles and reproduce observed behaviour in terms of layer detection distances.

4.1. Normal contact validation

Example scope

In this section a one-dimensional normal contact problem is used to validate the normal contact implementation. During the formulation of the method, two other simpler methods were explored but were found to give a poor representation of the contact conditions. These three contact methods are shown in Fig. 2. The method advocated for in this paper is referred to as the boundary GIMP method, presented in detail in Section 3, Fig. 1. The other two methods are: a centre GIMP method, where the rigid body interacts with the centre point of the GIMP domain, and a discrete MP method, where the deformable body is represented with standard MPs and the rigid body interacts with the discrete location of the MP.

Setup

The plane strain problem geometry is outlined in Fig. 3, where a rigid body is pressing into the side of domain of length 1 m and height h, where h is the background grid size with each cell initially populated with four equal distributed MPs. The background grid is uniform, therefore the number of elements in the x-direction is $1/h$ with a one element thickness in y. All sides of the domain, except where contact between the rigid body and the MPs is occurring, are roller boundary conditions. The material is elastic with Young's modulus $E = 1$ MPa, Poisson's ratio $\nu = 0$, and a corresponding normal penalty of $\epsilon_n = 20A_pE$, where A_p is defined in Section 3.5. The combination of the roller boundary conditions, the symmetry of the contact in y and $\nu = 0$ makes this problem one-dimensional. In total the rigid body was displaced 0.48 m into the sample which was divided into 24 steps, i.e. 0.02 m in each step.

Results discussion

The analytical solution of a column under compression can be expressed as

$$\sigma = E \log\left(\frac{l}{l_0}\right)\left(\frac{l_0}{l}\right). \tag{41}$$

l_0 is the original length of the deformable column and l is the current length. To investigate the convergence rate of the different contact formulations, h is varied, which changes the width of the sample in the y-direction. For an objective comparison the error in the stress field should be normalised with respect to the reference stress solution, leading to the volume-weighted normalised stress error being defined as

$$e = \left(\frac{\sum_{\forall p} |\sigma - \sigma_p|^2 V_p^0}{\sigma^2 \sum_{\forall p} V_p^0}\right)^{1/2}, \tag{42}$$

where p is referred to the point number, V_p^0 is the point's original volume and σ_p is the Cauchy stress at the point. For the convergence test the rigid body was by displaced 0.48 m, giving a deformed column length of $l = 0.52$ m.

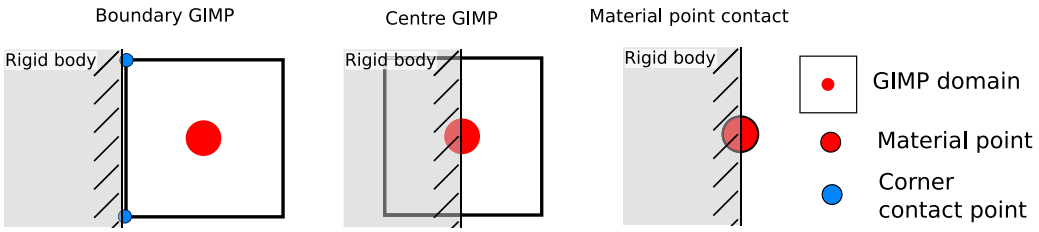

Fig. 2. Normal contact validation: potential contact formulations between a rigid body surface and a GIMP domain and a material point.

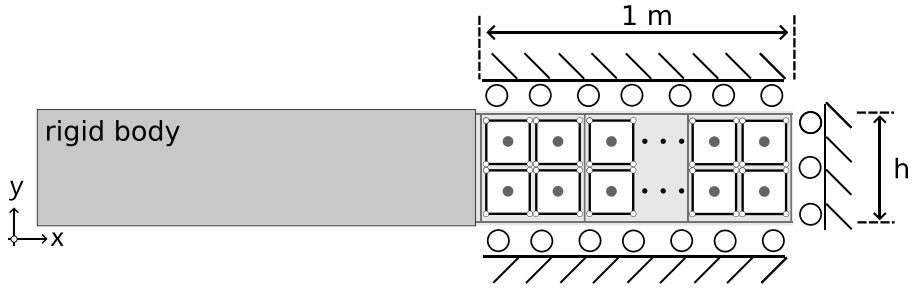

Fig. 3. Normal contact validation: Initial geometry.

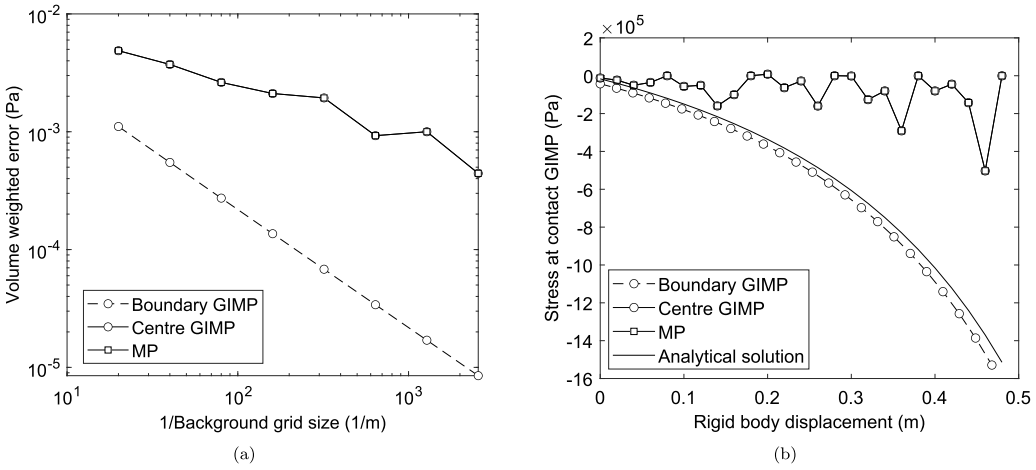

Fig. 4. Normal contact validation: (a) the error with refinement for a range of contact techniques for $l = 0.5$ m and (b) the variation stress of the GIMP/MP in contact with the rigid body with displacement for $h = 0.2$ m.

The variation of the error, e, with $1/h$ is shown in Fig. 4(a). The stress at contact of the GIMP or MP in contact with the rigid body is plotted in Fig. 4(b) for rigid body displacements $\in [0, 0.48]$ and $h = 0.2$ m. Both figures consider the three contact methods presented in Fig. 2. The first observation is that the boundary GIMP method has optimal convergence for stress error e, shown in Fig. 4(a), at a rate of 1.003. Additionally the stress solution of the GIMPM in contact with the rigid body is very close to the true solution with $h = 0.2$ m over the range of considered displacements, as shown in Fig. 4(b).

For the other two methods, centre GIMP and MP contact, the performance in the stress error convergence is sub-optimal, at a rate of 0.494. The cause of this reduction in the convergence rate is the stress error at the GIMP/MP in contact with the rigid body. This is shown in Fig. 4(b), where it is clear that stresses at the contact are highly oscillatory and not close to the analytical solution.

Due to the findings of this example the remainder of the paper adopts the Boundary GIMP contact method where the corners of the GIMP domain govern contact with the rigid body.

4.2. Tangential contact validation

Example scope

This section will demonstrate that the stick–slip friction algorithm provided in Section 3.4 combined with the GIMP corner contact correctly captures the stick–slip states of the Coulomb friction law.

Setup

The plane strain problem geometry is shown in Fig. 5(a), there is a rigid body wedge, with angle $\theta = 45°$, pressing into an elastic body, constructed with GIMPs, with a top surface also inclined at 45°.

The elastic body has side lengths $L_1 = 10$ m and $L_2 = 10.5$ m, its width is $W = 0.5$ m. It has a Young's Modulus $E = 1$ MPa and Poisson's ratio $\nu = 0.0$. The friction coefficient μ was varied with between 0 and 1.2, $\mu = 1$ had the corresponding friction angle of 45°. The experimental setup in Fig. 5(a) is such that if $\mu \geq 1$ then the global response should be stick, whereas if $\mu < 1$ the material should be slipping. Three mesh refinements are considered with element size $h = 0.5$, 0.25 and 0.125 m.

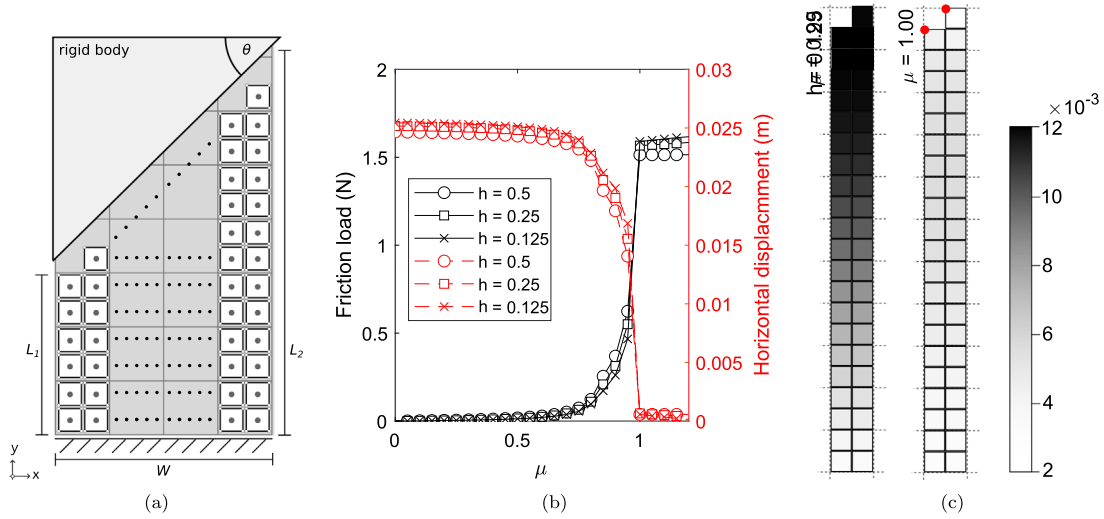

Fig. 5. Tangent contact validation: (a) shows the initial geometry, with the total frictional force and horizontal displacement of the contact face shown in (b), with the horizontal displacement distribution for $\mu = 0.95$ and $\mu = 1.00$ show in (c).

The rigid body is displaced 0.05 m into the deformable body with the total displacement occurring in one load step. The contact penalty values for this problem were set to

$$\epsilon_n = 20A_pE \quad \text{and} \quad \epsilon_t = 10A_pE,$$

where A_p is defined in Section 3.5.

Results discussion

The friction force and mean horizontal displacement are shown in Fig. 5(b), and as μ approaches 1 the fastest change in the load and displacement is observed. However once $\mu = 1$ there is little change, indicating that the majority of the contact is in the stick state. There are two contributing factors as to why full stick and slip is not observed. The first factor is that the boundary of the domain is not smooth, and hence an uneven contact force is observed across the boundary. This is most noticeable in the coarse case in Fig. 5(c), where the contact points, highlighted by the red dots, are weighted to the left of the domain. The second factor is that there is a rigid body impinging on a deformable body, hence the total vertical strain is not going to be constant across the sample. This could be resolved if the rigid body was deformable and had the same material properties and dimensions as the deformable body. Both these factors contribute to an almost stick state, and hence for $\mu > 1$ there is an increase in the tangential force as more contact points become stuck. However despite this, Fig. 5(a) shows that the horizontal displacement is significantly different when in slip, $\mu = 0.95$, compared to stick $\mu = 1$; for the most refined case the horizontal displacement for $\mu = 0.95$ and $\mu = 1$ was respectively 1.6×10^{-2} and 5.6×10^{-4} m.

4.3. CPT: validation

Example scope

In this section a Cone Penetration Test (CPT) is simulated numerically in axisymmetry. The predicted cone resistance is compared to experimental data obtained by Davidson et al. (2022), demonstrating that the proposed implicit method is sufficiently robust to model a demanding highly-nonlinear contact problem in geotechnics, and can achieve accurate results with respect to experiments. Background mesh/MP sensitivity and run-time performance analysis will also be discussed.

Material model

The material used in the real experiment was dry silica sand obtained from Congleton in the UK (Davidson et al., 2022). There are many sophisticated and well validated material models for sand in the literature, however these advanced material models often require many material parameters which can be problematic to obtain without access to specific laboratory test data and even with extensive datasets, some parameters often have to be assumed. Some advanced models specifically include sand grain crushing and the associated evolution of the particle size distribution (Einav, 2007; Shen and Buscarnera, 2022). However, significant crushing was not observed in the physical modelling (Davidson et al., 2022) and therefore this will not be considered in the numerical CPTs. The focus of this research is on modelling large deformation soil–structure interaction problems, specifically in the area of offshore geotechnics, and therefore the essential aspect of the material behaviour that must be captured is the ultimate state of the soil which can be achieved using a relatively simple constitutive model. From a practical point of view, offshore geotechnical site investigation often only delivers *in-situ* CPT data and limited core samples with uncertain stress history and sample disturbance, see Macdonald et al. (2023) for a study on subsea cores from the North Sea, UK. This research therefore focuses on using constitutive models that can be calibrated from CPT data, which excludes the use of the latest advanced sand models. It will be shown that a relatively simple material model can accurately predict large deformation soil–structure interaction provided key features of the soil behaviour are included. Due to the above points, the sand was modelled as an linear-elastic, perfectly-plastic material with a Drucker–Prager yield surface. This constitutive formulation has been selected as all of the required parameters can be estimated from the relative density of the material (which can be estimated from CPTs).

Most advanced material models include non-linear elasticity which requires several elasticity parameters. For example, some models use moduli for the initial response elastic response, and E_{50} as the secant modulus at 50% of the ultimate stress. Since the model here is linear-elastic the non-linear elastic response is approximated by adopting the E_{50} value as the constitutive model's Young's modulus. This approximation is often recommended in commercial software packages, e.g. the PLAXIS handbook (PLAXIS, 2010). The empirical model of Schanz et al. (2019) estimates Young's modulus via a reference $E_{50}^{ref} = 60R_D$ (in MPa), which is determined at a reference pressure of $p^{ref} = 100$ kPa where R_D is the relative density of the material. The initial state of the material is subject to gravity, therefore Young's modulus will vary

Table 1
Material properties.

Property	38%	82%
Reference Young's modulus, E_{50}^{ref} (kPa)	22,800	49,200
Density, ρ (kN/m^3)	16.5	18.2
Poisson's ratio	0.3	0.3
Friction angle (°)	32.8	38.3
Dilation angle (°)	2.8	8.3
Apparent cohesion (kPa)	0.3	0.3
Coefficient of earth pressure at rest, K_0	0.41	0.38
Stiffness exponent, m_E	0.56	0.44

Table 2
Scaled CPT geometry.

Dimension	Experiment	Scaled
Sample depth	434 mm	25 m
Sample radius	200 mm	12.5 m
Cone radius	8 mm	0.4 m

with depth and is calculated using the formula by Schanz et al. (2019) assuming a negligible cohesion

$$E_{50} = E_{50}^{ref}\left(\frac{\sigma_v K_0}{p^{ref}}\right)^{m_E} \qquad \text{with} \qquad \sigma_v = d_p\rho, \tag{43}$$

where $K_0 = 1 - \sin(\phi)$ is the coefficient of earth pressure at rest (Jaky, 1944), σ_v is the vertical stress and d_p is the distance of the MP from the surface of the sample (i.e. the depth), m_E is an exponent controlling the variation of stiffness with depth which can be estimated via relative density correlations provided by Brinkgreve et al. (2010)

$$m_E = 0.7 - 0.3125R_D.$$

E was kept constant during the simulation. This is an approximation. However, the results in Section 4.3 will demonstrate this approximation produces sufficiently accurate results. The friction, ϕ, and dilation, ψ, angles can be approximated by correlations provided by Brinkgreve et al. (2010)

$$\phi = 28 + 12.5R_D \qquad \text{and} \qquad \psi = -2 + 12.5R_D.$$

The dilation relationship permits negative dilation angles when the relative density of the sand falls below 16%, however the lowest relative density considered in this study was 38%. The experimental data corresponds to two homogeneous sand samples with relative density, loose at 38%, and, very dense at 82%. The material properties are given in Table 1 and were obtained using the above empirical formulae, with the exception of Poisson's ratio and apparent cohesion. The apparent cohesion was set at the very low value of 0.3 kPa as a compromise between numerical stability and the real material (dry sand) having zero cohesion. Poisson's ratio was taken as 0.3 as a representative value for this type of sand (Jefferies and Been, 2006).

Setup

To validate the GIMPM implementation, we compare numerical and experimental CPT results, the latter obtained by Davidson et al. (2022) where the CPT was conducted in a geotechnical centrifuge. The sand sample in the centrifuge experienced $40g$ at the top whilst the bottom of the sample experienced $50g$, the result being a greater effective depth, larger than the true depth, was experimented upon. The effective depth, d_e, is determined for this experiment

$$d_e = (10/0.4)d^2 + 40d$$

where d is the depth into the experimental sample. The geometry of the material sample and the CPT, for both the experiment and its corresponding scaling are provided in Table 2.

The axisymmetric domain and boundary conditions are shown in Fig. 6(a) with a illustration of the mesh shown in Fig. 6(b). The true mesh and GIMP distribution is shown in Fig. 6(c) with an expanded view of the refined region of the mesh shown in Fig. 6(d). On the bottom and right boundary roller boundary conditions are applied, on the left boundary there is no displacement constraint (homogeneous Neumann). In the formulation of the strain field for an axisymmetric analysis, if point is moved asymptotically close to axis an infinite strain field in the out of plane circumferential direction will be produced. This is in turn produces a very large stress field that resists material movement across the axis of symmetry. The mesh illustration in Fig. 6(b) shows that in the region of the elements shaded in dark grey are square with side length 0.1 m, All elements were initialised with 4 (2-by-2) GIMPs. The mesh was created using a power law to the size of the square light grey element, in the bottom right, with side lengths 2.85 m in x and 3.75 m in y.

In total the CPT was displaced 4 m into the sample which was divided into 80 equal load steps. The contact the penalty parameters were set to

$$\epsilon_n = 20A_pE_p \qquad \text{and} \qquad \epsilon_t = 10A_pE_p,$$

where A_p is defined in Section 3.5 and the coefficient of friction between the rigid body and the GIMPs was $\mu = 0.3$.

Results discussion

The results for the cone resistance are provided in Fig. 8(a), the first observation is that despite the relatively simple material model and the non-smooth representation of the boundary of the soil, the results agree well with the experimental data for both densities. However, the model does slightly over-predict the cone resistance compared to the experimental data. Additionally, despite the surface of the material being represented by points, rather than a smooth surface, the oscillations in the load are not significant. It shows that using the corners of the GIMP domains as points of contact provides clear and accurate results, however the magnitude of this oscillations are dependent on the number of material points in the domain.

A plot of the vertical stress for relative density 38% is shown in Figs. 7(a) and 7(b). For the application contact boundary condition the corners of the GIMP domains, rather then the centre, was to ensure that the boundary conditions were applied at the edge of the material domain. In Section 4.1 it was shown for a 1D problem that stress oscillations a the boundary were removed, Fig. 7(a) shows that this is also the case for a more complicated problem with vertical stress going from most compressive at the point of contact and reducing in compression the further away the point of contact.[5] The oscillations in the results in Fig. 8(a), are due to the boundary being represented by point-data, rather than a continuous surface. A study was performed to investigate how the cone resistance oscillations are effected by mesh refinement and number of material points. Three meshes are considered, the most refined was the same mesh and GIMP distribution as in Fig. 7(b), then two coarser meshes considered where the element sizes were approximately derefined so the elements were approximately $1/0.5$ and $1/0.3$ times larger. The number of material points per element were kept constant for all meshes. Fig. 8(b) shows tip pressure with depth for these refinements, the coarsest mesh refinement produces the largest stress oscillations, as the mesh is refined the oscillations reduce showing convergence to a smoother result. The time for the three mesh refinements for relative densities 38% and 82% are shown in Table 3. The computation was performed on the serial code on a computer with 3.25 GHz processor and 16 Gb of RAM. The code itself is written in MATLAB, and is an adaptation of AMPLE (Coombs and Augarde, 2020). Even for the most refined meshes the computational time is reasonable, with the refinement level of 0.5 showing a good compromise between computational time and stress oscillations.

[5] Note that the image has oversized GIMPs, this extenuates the apparent overlap between the cone penetrometer and the GIMP domains.

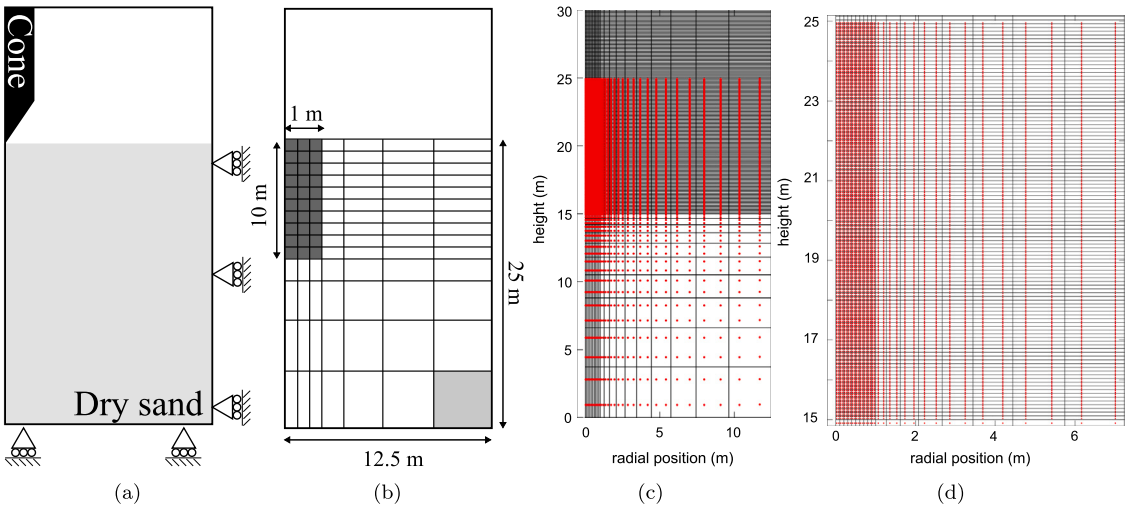

Fig. 6. CPT Validation: (a) shows the boundary conditions to the domain with a not-to-scale background mesh shown in (b). The true mesh and GIMP distribution is shown in (c) with a zoomed view of the refinement area shown in (d).

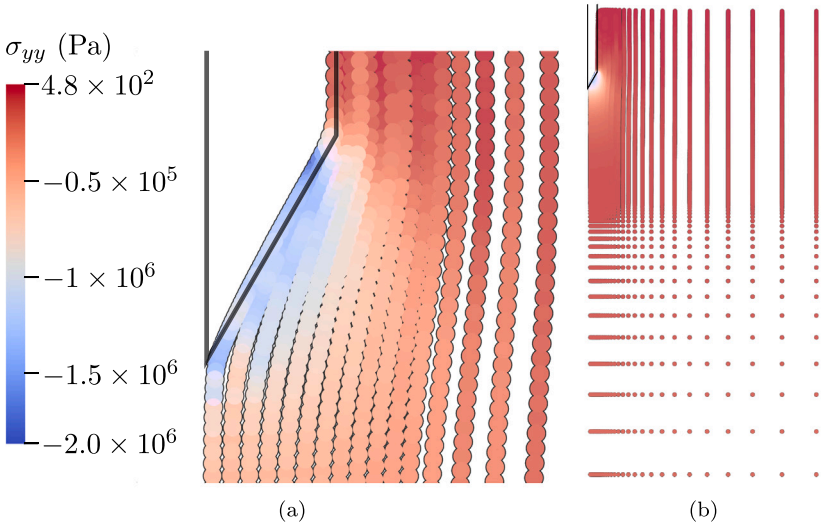

Fig. 7. CPT Validation: (a) is zoomed in view of the vertical stress field σ_{yy} around the CPT, the full stress field is shown in (b).

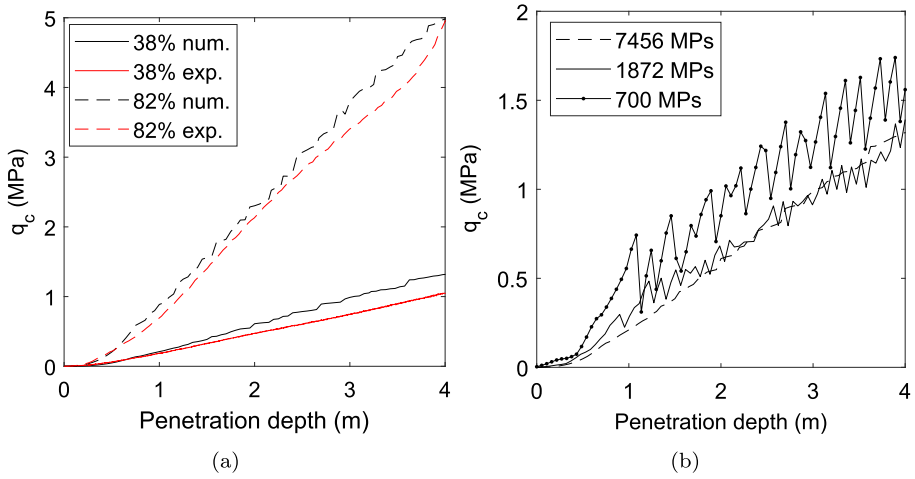

Fig. 8. CPT Validation: (a) shows the cone resistance as a function of depth for relatively densities 38% and 82% compared to experimental data from Robinson et al. (2021) and (b) is the cone resistance as a function of tip penetration for a sand with relative density 38% for a series of refinements.

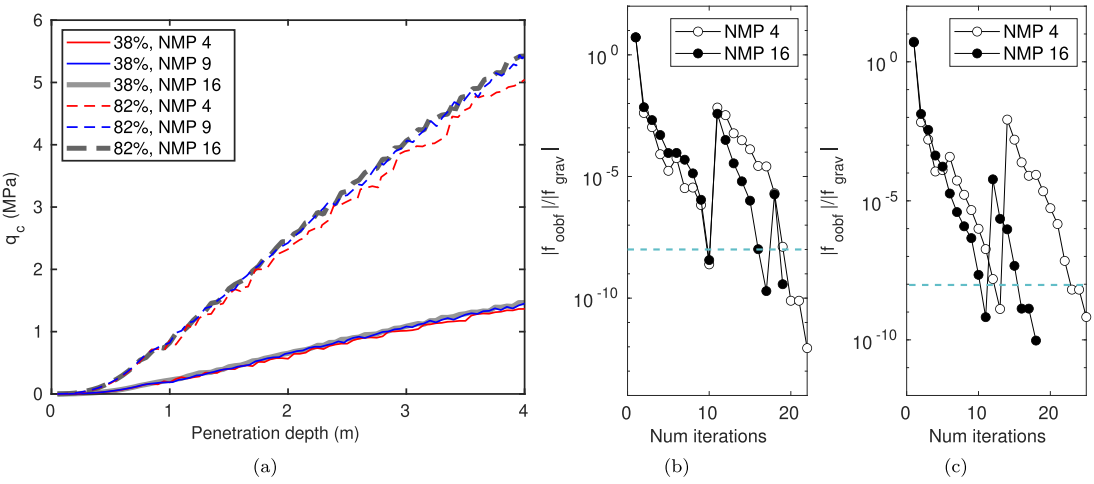

Fig. 9. Material point density: (a) shows the variation in results for sand with relative densities 38% and 82% when using different NMP values, whilst (b) and (c) shows the worst NR-scheme convergence for relative densities 38% and 82%, for NMP values 4 and 16.

Table 3
CPT validation: computational times.

Refinement level	0.3	0.5	1
Number of MPs	700	1872	7456
Computational time for 38% (min)	3.4	8.5	33.2
Computational time for 82% (min)	5.7	9.6	58.5

4.4. CPT: algorithmic performance

Example scope

This section reviews two aspects of the proposed numerical modelling framework using the CPT case described in the previous section as the physical problem. The first of these is the material point density — the ratio of the number of material points to number of elements. The second assesses how well the penalty method is performing, since the contact conditions are enforced weakly.

Material point density

For the CPT analyses presented in the previous section, the q_c results with depth, shown in Fig. 8(a), achieved good agreement with the experimental results. It was also shown that uniformly refining the mesh improved the smoothness of q_c result, see Fig. 8(b). However, it has been well documented that the stability of the solution is sensitive to the initial number of material points per element (NMP). This is due to both poor integration in the bulk of material from poorly placed MPs for integration and/or the small cut issue (Coombs, 2023b). If there is poor integration in the material bulk this can affect the stability of the NR scheme, the result is that the method does not converge. Additionally, poor integration can generally produce a poor result. Therefore the NMP is a compromise; there needs to be sufficient MPs such that the effects of poor integration are mitigated but not so many MPs that run time is excessive. To investigate the effect of NMP, the most refined mesh from Section 4.3 is used to model a CPT with 38% and 82% relative density sand. NMP is varied between 4, 9 and 16, corresponding to 2, 3 and 4 material points in each direction in each initially populated element.

The results for q_c with depth for varying numbers of MPs for both relatively densities are shown in Fig. 9(a). For all values of NMP the results are similar for their respective relative densities, with a general trend that the results converge with increasing NMP and that the results become smoother. Fig. 9(a) also demonstrates that despite NMP having an effect on the result, the effect is small with no scope for fortuitous agreement with the experimental result by selection of a specific NMP.

The second feature that NMP can affect is the stability of the NR scheme. This is considered in Figs. 9(b) and 9(c) for relative densities 38% and 82%, respectively. The figures show the results for the slowest converging load steps over each of the simulations for the respective sand densities. The convergence criterion set for the NR-scheme is

$$\frac{\|f_{oobf}\|}{\|f_{grav}\|} < 10^{-8}$$

f_{oobf} is the out-of-balance force vector, and f_{grav} denotes the external forces associated with the gravitational load. The value 10^{-8} is denoted by the blue dashed line in Figs. 9(b) and 9(c). The figures show a similar convergence pattern for both values of NMP. The sudden increases in the force residual are caused by new MP-rigid body contacts being detected. When this occurs the number of NR iterations is reset but it can been seen that all of the load steps take a reasonable number of iterations (less than 10) to converge each time new contact is detected. The figure shows that the stability of the algorithm is similar for 4 and 16 NMP.

Contact analysis

In this section, two aspects of contact are analysed: (i) the kinematics of the GIMPs interacting with the rigid body, and (ii) the length of interpenetration occurring during the simulation.

Figs. 10(c) to 10(c) shows what happens in a typical load step with GIMPs (shown by the grey shaded quadrilaterals) interacting with the rigid body (shown by the red line) on a background grid (shown by the blue lines). Fig. 10(a) shows the state before the rigid body is displaced vertically downwards. In Fig. 10(b) the rigid body has been moved downwards, with the highest deformation observed with the GIMPs in contact with the rigid body. It is important to highlight that the corners of the GIMPs, corresponding to the boundary of the material, are satisfying the contact boundary condition with only a small amount of interpenetration, which will be dependent on the magnitude of the normal penalty parameter. Once equilibrium has been found the GIMPs need to be updated and the edges of the GIMP domains aligned with the global coordinates (see Fig. 10(c)). In this case the GIMP domains are updated using the corner update rule proposed by Coombs et al. (2020). In this approach the corners of the domains are updated according to the background grid deformation and the finite element basis functions at the corner points, the new extent of the domain defined by a rectangle aligned with the global axes intersecting the mid edges of this updated quadrilateral. Finally the size of the domain is uniformly scaled to maintain consistency between the volume ratio (the determinant of the deformation gradient) and the domain size (see Coombs et al. (2020) for details). This domain updating approach is preferred as it does not suffer from the spurious artefacts known to affect some

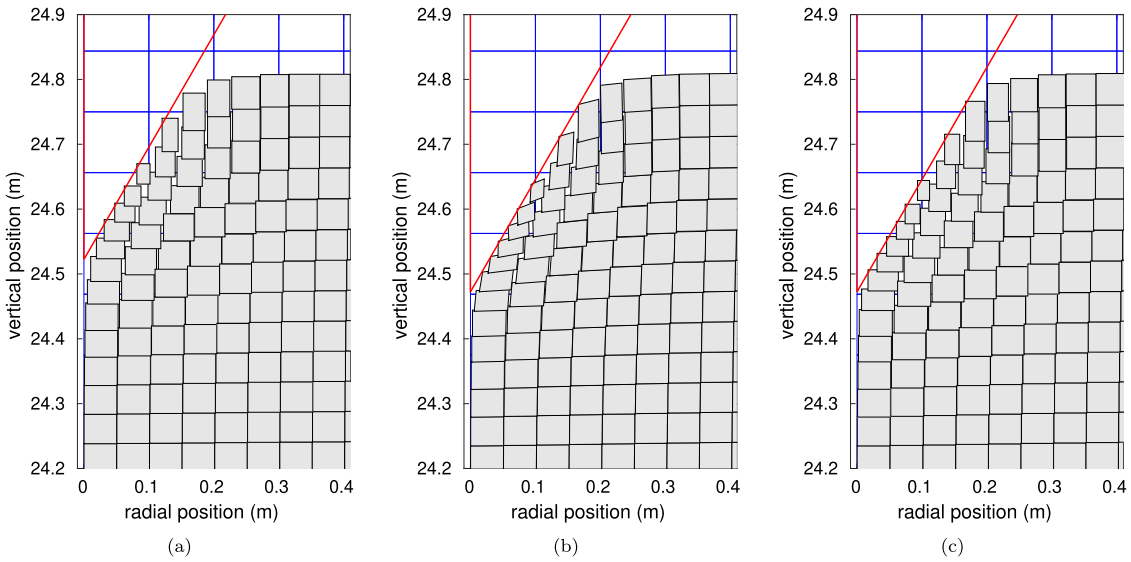

Fig. 10. Contact analysis: GIMP and rigid positions and deformations at the point before a load step is started (a), the converged position of the rigid body and GIMP domains at the end of a load step, and (c) the updated positions of the GIMP domains using the corner method by Coombs et al. (2020).

Table 4
Maximum interpenetration depths relative to CPT diameter of 0.8 m for varying relative densities and number of initial material points (NMP) per element.

NMP	Relative interpenetration	
	38%	82%
4	0.033	0.050
9	0.028	0.044
16	0.025	0.044

Table 5
Layered soil CPT: List of experiments.

Experiment	Material	
	Top 5 m	Buried sample
A	38%	38%
B	82%	82%
C	38%	82%
D	82%	38%

other domain updating approaches under certain deformation modes, including large shearing (Coombs et al., 2020).

For the CPT results with the different numbers of MPs per element presented in Fig. 9(a), the maximum interpenetration of the GIMPs with respect to the CPT diameter, 0.8 m, is provided in Table 4. The table shows that the interpenetration of the GIMPs with the rigid body are small and decreases with increasing NMP. However it is noted that the interpenetration increases slightly with relative density, this could resolved by using a higher penalty value.

4.5. CPT: layered soils

Example scope

The capability of the method to model a layered sand and reproduce features which are present in experimental data are explored in this section. The purpose of this experiment is to demonstrate that the contact methodology presented this is paper is robust and able to simulate contact with materials that have a large range of properties and therefore show that the method is a reliable tool for more realistic problems. In this section, comparisons with existing literature are presented to demonstrate the model's ability to incorporate the effect of sand below the interface to affect the cone resistance above the interface. This is a study on the ability of the model to detect these effects and comparisons are made to show that the results are reasonable.

Setup

The geometry and discritisation for the simulations in this section are the same as in 4.3. The material distribution was different, with one sand type in the top 5 m of the sample, correspond to a depth of 12.5 times the cone radius, and another sand type in the remainder of the sample. Additionally, the total cone penetration depth was extended to 10 m. In total four numerical experiments were run, shown in Table 5, two layered samples and two homogeneous samples, which acted as references to the layered material.

The rigid body displacement of 10 m was divided by 200 equal load steps, the coefficient of friction between the rigid body and the GIMPs was set to $\mu = 0.3$. The contact penalty parameters were set to

$$\epsilon_n = 20 A_p E_p \quad \text{and} \quad \epsilon_t = 10 A_p E_p,$$

where A_p is defined in Section 3.5.

Result discussion

The results in Fig. 11 show how the tip pressure varies with relative depth for the soil samples provided in Table 5. For both the layered sands there are three stages to the result. Up to a distance of ≈2.5 radii of the cone tip from the interface the layered and homogeneous result are the same for the respect sand the cone is currently in. However, within ≈2.5 radii the results start to diverge and there is a transition zone where the layered cone resistance results are far from the homogeneous result. Then after a penetration of a further ≈3 radii of the tip into the buried layer the cone resistance begins to asymptote to the homogeneous sand result.

Overall the trend of the result is similar to the observations for sands, Xiao et al. (2023), Tehrani et al. (2018) and clay (Walker and Yu, 2010). Xiao et al. (2023) and Tehrani et al. (2018) note that the detection distance, both before and after the interface, is dependent on the density of the buried sample and layer order (loose over dense, or dense over loose). The results presented are within the range of detection distance of ≈2 and ≈4 radii for buried loose and dense soils respectively observed in Xiao et al. (2023) but outside the range proposed by Tehrani et al. (2018) which is likely due to their increased penetration depth and surcharge. A full study is required to understand the mechanics of the multiple layers and the effect on the global

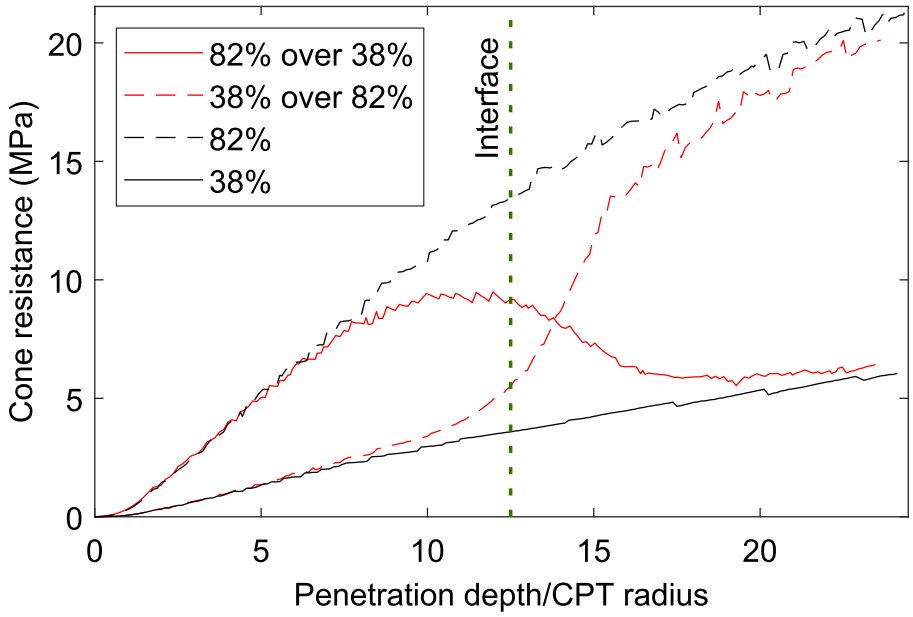

Fig. 11. Layered soil CPT: Cone resistance with penetration depth for soil layers defined in Table 5.

response in order to validate layered response and is therefore beyond the scope here. However, Fig. 11 does demonstrate the stability of the method to model problems with material interfaces, particularly it demonstrates the stability when there are multiple materials in contact with he rigid body. Additionally the oscillations in the result remain small for this deep penetration.

5. Conclusion

This paper has presented a consistent contact methodology between a continuum body modelled with the GIMPM and a rigid body within an implicit pseudo-static framework with a focus on a validated methodology against experimental data, ensuring its reliability and applicability. The novelty of the method is that it uses the definition of individual GIMP domains to define the boundary. This has two advantages. Firstly, there is no need to construct the boundary for contact, thus avoiding unnecessary expense. Secondly, the contact constraints are applied consistently in that they are correctly applied on the boundary of the domain. The result of making this consistent is highlighted clearly in a normal contact validation. Incorrect definitions of the boundaries are shown to have sub-optimal convergence rates and highly oscillatory behaviour at the point of contact, whereas the method presented here shows optimal convergence with a smooth stress field. The method, including a global Newton–Raphson algorithm is also described and validated to accurately capture stick–slip behaviour. Furthermore, the GIMPM coupled with the contact model is thoroughly validated against experimental data from a CPT. A range of sand relative densities have been considered and a very good agreement between the numerical and experimental results achieved. Furthermore in these more complicated simulations no oscillatory behaviour was observed at the contact boundary of the deformable body. This means that accurate observations of stress fields around CPTs is possible with this method. Lastly the model was used to simulate layered sand media, reproducing features such as pre-sensing of the layer boundary with the cone resistance.

As well as the correct application of the contact constraints, a significance of this modelling approach is that it is implicit. Solving the system implicitly means that large load, or displacement, increments can be applied. It was shown with the CPT simulation, using an unoptimised serial MATLAB code could achieve results with a reasonable accuracy with 10 min, and a high accuracy between 30 min to 1 h. This is significant because it permits the possibility to quickly run large parameter sweeps, and the scope of the parameter sweeps could very large if the code was optimised.

CRediT authorship contribution statement

Robert E. Bird: Writing – review & editing, Writing – original draft, Validation, Software, Methodology, Data curation, Conceptualization. **Giuliano Pretti:** Writing – review & editing, Writing – original draft, Software, Conceptualization. **William M. Coombs:** Writing – review & editing, Writing – original draft, Supervision, Funding acquisition, Conceptualization. **Charles E. Augarde:** Writing – review & editing, Writing – original draft, Supervision, Funding acquisition, Conceptualization. **Yaseen U. Sharif:** Writing – review & editing, Data curation, Conceptualization. **Michael J. Brown:** Writing – review & editing, Funding acquisition, Data curation, Conceptualization. **Gareth Carter:** Writing – review & editing, Funding acquisition, Conceptualization. **Catriona Macdonald:** Writing – review & editing, Funding acquisition, Conceptualization. **Kirstin Johnson:** Writing – review & editing, Funding acquisition, Conceptualization.

Declaration of competing interest

The authors declare that they have no known competing financial interests or personal relationships that could have appeared to influence the work reported in this paper.

Data availability

Data available at http://doi.org/10.15128/r1tt44pm87t.

Acknowledgements

This work was supported by the Engineering and Physical Sciences Research Council, United Kingdom [grant numbers EP/W000970/1, EP/W000997/1 and EP/W000954/1]. The second author is supported by funding from the Faculty of Science, Durham University. All data produced in this paper is available at http://doi.org/10.15128/r1tt44pm87t.

References

Bardenhagen, S.G., Brackbill, J.U., Sulsky, D., 2000. The material-point method for granular materials. Comput. Methods Appl. Mech. Engrg. 187 (3–4), 529–541.

Bardenhagen, S.G., Guilkey, J., Roessig, K.M., Brackbill, J.U., Witzel, W.M., Foster, J.C., 2001. An improved contact algorithm for the material point method and application to stress propagation in granular material. CMES Comput. Model. Eng. Sci. 2 (4), 509.

Bardenhagen, S.G., Kober, E.M., 2004. The generalized interpolation material point method. Comput. Model. Eng. Sci. 5 (6), 477–496.

Bing, Y., Cortis, M., Charlton, T.J., Coombs, W.M., Augarde, C.E., 2019. B-spline based boundary conditions in the material point method. Comput. Struct. 212, 257–274.

Bird, R., Coombs, W.M., Augarde, C., Brown, M., Sharif, Y., Carter, G.D.O., Johnson, K., Macdonald, C., 2023. Cone penetration tests (CPTs) in layered soils: a material point approach. In: Numerical Methods in Geotechnical Engineering 2023.

Bisht, V., Salgado, R., Prezzi, M., 2021. Material point method for cone penetration in clays. J. Geotech. Geoenviron. Eng. 147 (12), 04021158.

Brinkgreve, R.B.J., Engin, E., Engin, H.K., 2010. Validation of empirical formulas to derive model parameters for sands. In: Numerical Methods in Geotechnical Engineering. pp. 137–142.

Burman, E., 2010. Ghost penalty. C. R. Math. 348 (21), 1217–1220.

Charlton, T.J., Coombs, W.M., Augarde, C.E., 2017. iGIMP: An implicit generalised interpolation material point method for large deformations. Comput. Struct. 190, 108–125.

Chen, Z-P., Zhang, X., Qiu, X-M., Liu, Y., 2017. A frictional contact algorithm for implicit material point method. Comput. Methods Appl. Mech. Engrg. 321, 124–144.

Ciantia, M.O., Arroyo, M., Butlanska, J., Gens, A., 2016. DEM modelling of cone penetration tests in a double-porosity crushable granular material. Comput. Geotech. 73, 109–127.

Coombs, W.M., 2023a. A ghost-stabilised material point method for large deformation geotechnical analysis. In: Zdravkovic, L., Konte, S., Taborda, D.M.G., Tsiampousi, A. (Eds.), 10th European Conference on Numerical Methods in Geotechnical Engineering.

Coombs, W.M., 2023b. Ghost stabilisation of the material point method for stable quasi-static and dynamic analysis of large deformation problems. Internat. J. Numer. Methods Engrg. 124 (21), 4841–4875.

Coombs, W.M., Augarde, C.E., 2020. AMPLE: a material point learning environment. Adv. Eng. Softw. 139, 102748.

Coombs, W.M., Augarde, C.E., Brennan, A.J., Brown, M.J., Charlton, T.J., Knappett, J.A., Ghaffari Motlagh, Y., Wang, L., 2020. On Lagrangian mechanics and the implicit material point method for large deformation elasto-plasticity. Comput. Methods Appl. Mech. Engrg. 358, 112622.

Cortis, M., Coombs, W.M., Augarde, C.E., Brown, M., Brennan, A., Robinson, S., 2018. Imposition of essential boundary conditions in the material point method. Internat. J. Numer. Methods Engrg. 113 (1), 130–152.

Curnier, A., He, Q., Klarbring, A., 1995. Continuum mechanics modelling of large deformation contact with friction. Contact Mech. 145–158.

Davidson, C., Brown, M., Cerfontaine, B., Knappett, J., Brennan, A., Al-Baghdadi, T., Augarde, C.E., Coombs, W.M., Wang, L., Blake, A., Richards, D., Ball, J.D., 2022. Physical modelling to demonstrate the feasibility of screw piles for offshore jacket supported wind energy structures. Géotechnique 72 (2), 108–126.

Einav, I., 2007. Breakage mechanics—Part I: Theory. J. Mech. Phys. Solids 55 (6), 1274–1297.

Gan, Y., Sun, Z., Chen, Z., Zhang, X., Liu, Y., 2018. Enhancement of the material point method using B-spline basis functions. Internat. J. Numer. Methods Engrg. 113 (3), 411–431.

Gao, L., Guo, N., Yang, Z.X., Jardine, R.J., 2022. MPM modeling of pile installation in sand: Contact improvement and quantitative analysis. Comput. Geotech. 151, 104943.

Gavin, N.D., 2024. Case in Points: Developing a Patient-specific Model of the Human Left Ventricle using the Material Point Method (Ph.D. thesis). Durham University.

Ghasemi, P., Calvello, M., Martinelli, M., Galavi, V., Cuomo, S., 2018. MPM simulation of CPT and model calibration by inverse analysis. In: Cone Penetration Testing 2018. CRC Press, pp. 295–301.

Gonzalez Acosta, J.L., Vardon, P.J., Hicks, M.A., 2021. Development of an implicit contact technique for the material point method. Comput. Geotech. 130, 103859.

González Acosta, J.L., Vardon, P.J., Remmerswaal, G., et al., 2020. An investigation of stress inaccuracies and proposed solution in the material point method. Comput. Mech. 65, 555–581.

Hauser, L., Schweiger, H.F., 2021. Numerical study on undrained cone penetration in structured soil using G-PFEM. Comput. Geotech. 133, 104061.

Hu, Y., Fang, Y., Ge, Z., Qu, Z., Zhu, Y., Pradhana, A., Jiang, C., 2018. A moving least squares material point method with displacement discontinuity and two-way rigid body coupling. ACM Trans. Graph. 37 (4), 1–14.

Jaky, J., 1944. The coefficient of earth pressure at rest. J. Soc. Hung. Archit. Eng..

Jefferies, M., Been, K., 2006. Soil Liquefaction: A Critical State Approach. CRC Press.

Khosravi, A., Martinez, A., DeJong, J.T., 2020. Discrete element model (DEM) simulations of cone penetration test (CPT) measurements and soil classification. Can. Geotech. J. 57 (9), 1369–1387.

Lei, Z., Wu, B., Wu, S., Nie, Y., Cheng, S., Zhang, C., 2022. A material point-finite element (MPM-FEM) model for simulating three-dimensional soil-structure interactions with the hybrid contact method. Comput. Geotech. 152, 105009.

Liang, Y., Given, J., Soga, K., 2023. The imposition of nonconforming Neumann boundary condition in the material point method without boundary representation. Comput. Methods Appl. Mech. Engrg. 404, 115785.

Liu, C., Sun, W., 2020. ILS-MPM: An implicit level-set-based material point method for frictional particulate contact mechanics of deformable particles. Comput. Methods Appl. Mech. Engrg. 369, 113168.

Lu, K., Augarde, C.E., Coombs, W.M., Hu, Z., 2019. Weak impositions of Dirichlet boundary conditions in solid mechanics: A critique of current approaches and extension to partially prescribed boundaries. Comput. Methods Appl. Mech. Engrg. 348, 632–659.

Ma, J., Wang, D., Randolph, M.F., 2014. A new contact algorithm in the material point method for geotechnical simulations. Int. J. Numer. Anal. Methods Geomech. 38 (11), 1197–1210.

Macdonald, C., Carter, G.D.O., Johnson, K.R., Augarde, C.E., Coombs, W.M., Bird, R.E., Brown, M.J., Sharif, Y.U., 2023. Depth of lowering and layered soils; a case study from across the north sea.. In: Offshore Site Investigation Geotechnics 9th International Conference Proceeding. Vol. 2096, Society for Underwater Technology, pp. 2096–2103.

Martinelli, M., Galavi, V., 2021. Investigation of the material point method in the simulation of cone penetration tests in dry sand. Comput. Geotech. 130, 103923.

Martinelli, M., Pisanò, F., 2022. Relating cone penetration resistance to sand state using the material point method. Géotech. Lett. 12 (2), 131–138.

Martinelli, M., Vahid, G., 2021. Investigation of the material point method in the simulation of cone penetration tests in dry sand. Comput. Geotech. 130, 103923.

Mast, C.M., Mackenzie-Helnwein, P., Arduino, P., Miller, G.R., 2011. Landslide and Debris flow-induced static and dynamic loads on protective structures. In: Borja, R.I. (Ed.), Multiscale and Multiphysics Processes in Geomechanics. Springer Berlin Heidelberg, pp. 169–172.

Monforte, L., Arroyo, M., Carbonell, J.M., Gens, A., 2017. Numerical simulation of undrained insertion problems in geotechnical engineering with the Particle Finite Element Method (PFEM). Comput. Geotech. 82, 144–156.

Nakamura, K., Matsumura, S., Mizutani, T., 2021. Particle-to-surface frictional contact algorithm for material point method using weighted least squares. Comput. Geotech. 134, 104069.

Phuong, N.T.V., van Tol, A.F., Elkadi, A.S.K., Rohe, A., 2016. Numerical investigation of pile installation effects in sand using material point method. Comput. Geotech. 73, 58–71.

Pietrzak, G., Curnier, A., 1999. Large deformation frictional contact mechanics: continuum formulation and augmented Lagrangian treatment. Comput. Methods Appl. Mech. Engrg. 177 (3–4), 351–381.

PLAXIS, 2010. PLAXIS V.9 Material Models Manual. Bentley Systems.

Pretti, G., 2024. Continuum Mechanics and Implicit Material Point Method to Underpin the Modelling of Drag Anchors for Cable Risk Assessment (Ph.D. thesis). Durham University.

Pretti, G., Bird, R.E., Gavin, N.D., Coombs, W.M., Augarde, C.E., 2024. A stable poro-mechanical formulation for material point methods leveraging overlapping meshes and multi-field ghost penalisation. arXiv:2405.12814.

Remmerswaal, G., 2017. Development and Implementation of Moving Boundary Conditions in the Material Point Method (Master's thesis). TU Delft.

Remmerswaal, G., 2023. The Random Material Point Method for Assessment of Residual Dyke Resistance: Investigating the Influence of Soil Heterogeneity on Slope Failure Processes (Ph.D. thesis). Delft University of Technology.

Robinson, S., Brown, M.J., Matsui, H., Brennan, A., Augarde, C.E., Coombs, W.M., Cortis, M., 2021. A cone penetration test (CPT) approach to cable plough performance prediction based upon centrifuge model testing. Can. Geotech. J. 58 (10), 1466–1477.

Sadeghirad, A., Brannon, R.M., Burghardt, J., 2011. A convected particle domain interpolation technique to extend applicability of the material point method for problems involving massive deformations. Int. J. Numer. Methods Eng. 86 (12), 1435–1456.

Schanz, T., Vermeer, P.A., Bonnier, P.G., 2019. The hardening soil model: Formulation and verification. In: Beyond 2000 in Computational Geotechnics. Routledge, pp. 281–296.

Shen, X., Buscarnera, G., 2022. Fabric-enriched continuum breakage mechanics (F-CBM). Geotechnique 73 (11), 1015–1030.

Simo, J.C., Laursen, T.A., 1992. An augmented Lagrangian treatment of contact problems involving friction. Comput. Struct. 42 (1), 97–116.

Sticko, S., Ludvigsson, G., Kreiss, G., 2020. High-order cut finite elements for the elastic wave. Adv. Comput. Math. 46 (45), 1–28.

Sulsky, D., Chen, Z., Schreyer, H.L., 1994. A particle method for history-dependent materials. Comput. Methods Appl. Mech. Engrg. 118 (1–2), 179–196.

Sulsky, D., Zhou, S.-J., Schreyer, H.L., 1995. Application of a particle-in-cell method to solid mechanics. Comput. Phys. Comm. 87 (1), 236–252.

Tehrani, F.S., Arshad, M.I., Prezzi, M., Salgado, R., 2018. Physical modeling of cone penetration in layered sand. J. Geotech. Geoenviron. Eng. 144 (1), 04017101.

Tolooiyan, A., Gavin, K., 2011. Modelling the cone penetration test in sand using cavity expansion and arbitrary Lagrangian Eulerian finite element methods. Comput. Geotech. 38 (4), 482–490.

Walker, J., Yu, H-S, 2010. Analysis of the cone penetration test in layered clay. Géotechnique 60 (12), 939–948.
Wang, D., Bienen, B., Nazem, M., Tian, Y., Zheng, J., Pucker, T., Randolph, M.F., 2015. Large deformation finite element analyses in geotechnical engineering. Comput. Geotech. 65, 104–114.
Wang, L., Coombs, W.M., Augarde, C.E., Cortis, M., Brown, M.J., Brennan, A.J., Knappett, J.A., Davidson, C., Richards, D., White, D.J., et al., 2021. An efficient and locking-free material point method for three-dimensional analysis with simplex elements. Internat. J. Numer. Methods Engrg. 122 (15), 3876–3899.
Wriggers, P., 2006. Computational Contact Mechanics. Springer.
Xiao, L., Lu, L., Wang, Z., He, B., Arai, K., 2023. Estimation of the detection distances of CPT resistance. Eng. Geol. 313, 106953.
Yamaguchi, Y., Moriguchi, S., Terada, K., 2021. Extended B-spline-based implicit material point method. Internat. J. Numer. Methods Engrg. 122 (7), 1746–1769.
Yost, K.M., Martinelli, M., Yerro, A., Green, R.A., de Lange, D.A., 2023. Addressing complexities in MPM modeling of calibration chamber cone penetrometer tests in homogenous and highly interlayered soils. Comput. Geotech. 158, 105378.